Nanometer-scale mapping of irreversible electrochemical nucleation processes on solid Li-ion electrolytes

Published in:
Scientific Reports

Document Version:
Publisher's PDF, also known as Version of record

Queen's University Belfast - Research Portal:
Link to publication record in Queen's University Belfast Research Portal

SCIENTIFIC REPORTS

Nanometer-scale mapping of irreversible electrochemical nucleation processes on solid Li-ion electrolytes

Amit Kumar[1], Thomas M. Arruda[1], Alexander Tselev[1], Ilia N. Ivanov[1], Jamie S. Lawton[2], Thomas A. Zawodzinski[2], Oleg Butyaev[3], Sergey Zayats[3], Stephen Jesse[1] & Sergei V. Kalinin[1]

[1]Center for Nanophase Materials Sciences, Oak Ridge National Laboratory, Oak Ridge, TN, USA, [2]Department of Chemical and Biomolecular Engineering, University of Tennessee Knoxville, Knoxville, TN, USA, [3]NT-MDT America, Santa Clara, CA, USA.

Electrochemical processes associated with changes in structure, connectivity or composition typically proceed via new phase nucleation with subsequent growth of nuclei. Understanding and controlling reactions requires the elucidation and control of nucleation mechanisms. However, factors controlling nucleation kinetics, including the interplay between local mechanical conditions, microstructure and local ionic profile remain inaccessible. Furthermore, the tendency of current probing techniques to interfere with the original microstructure prevents a systematic evaluation of the correlation between the microstructure and local electrochemical reactivity. In this work, the spatial variability of irreversible nucleation processes of Li on a Li-ion conductive glass-ceramics surface is studied with $\sim$30 nm resolution. An increased nucleation rate at the boundaries between the crystalline $AlPO_4$ phase and amorphous matrix is observed and attributed to Li segregation. This study opens a pathway for probing mechanisms at the level of single structural defects and elucidation of electrochemical activities in nanoscale volumes.

Progress in nanoscience and nanotechnology, the hallmarks of science in twenty first century, hinges upon the capability to probe and control ionic and electrochemical phenomena on nanometer scales. During the first decades of nanoscience, tremendous progress was achieved in understanding the mechanical, transport, magnetic, and structural materials functionalities down to the nanometer scale, enabled by the development of scanning probe techniques (SPM), electron microscopy and other characterization techniques. Equally impressive are recent advances in nanofabrication which lie at the foundation of modern information technologies[1] and also enable studies of fundamental physical phenomena. However, nanoscale probing and manipulation of matter through electrical currents - a key step towards development of techniques for probing of local ionic transport behavior as well as local electrochemical reactions - remains a challenge. This progress is required for breakthroughs in applications ranging from energy storage[2] and conversion to electrochemical actuation[3] to nanofabrication[4–6], and will potentially enable new and serendipitous areas of science and technology.

Electrochemical processes associated with significant changes in material structure, lattice connectivity or composition (e.g. electroforming in memristors[7] or initial stages of electrodeposition[5,8,9]) typically proceed through the stage of new phase nucleation with subsequent growth of nuclei[10]. The nucleation stage determines the uniformity, direction and nature of the final product[11]. Hence, a first step towards understanding and controlling reactions by currents is the elucidation and eventual control of the nucleation mechanism. Despite some recent progress[5,8,12], factors controlling nucleation kinetics and thermodynamics, including the interplay between local mechanical conditions, microstructure and local ionic profile remained inaccessible. Furthermore, the tendency of current probing techniques to interfere with the original microstructure prevents a systematic evaluation of the correlation between the microstructure and local electrochemical reactivity. Here, we demonstrate the use of a current-based SPM technique for high resolution mapping of local reactivity and the mechanism of nucleation processes in local electrochemical reactions, mirroring recent advances for single-molecule reactions by force spectroscopy.

As a model system, we have chosen commercially available Li-ion conducting glass ceramics (LICGC) with the general composition: $Li_2O–Al_2O_3–SiO_2–P_2O_5–TiO_2–GeO_2$[13,14]. This material has high Li–ion conductivity at room temperature ($\sim$1 $\times$ 10^{-4} S cm^{-1}) and no electronic conductance, hence is being extensively studied as a suitable solid electrolyte for Li-air and Li-water batteries[15]. In the context of this work, LICGC offers an advantage of high surface stability with respect to water and oxygen, enabling studies in ambient and glove-box

environments (unlike many others including cathodes, anodes and other electrolytes for which surface degradation is inevitable even at ppm levels of O_2 and H_2O).

Previously, we have explored micron scale (1–2 μm) particle formation during Li-ion reduction on the surface of LICGC and have shown that the reduction is partially reversible under inert conditions[16,17]. The transference number, which represents the ratio of the Li atoms plated and electrons transferred during the reduction is close to unity when experiments are conducted under an Ar atomosphere. However, these studies - as well as those from Krumpelmann *et al.*[18] - were necessarily limited to large length scales resulting in large particles (~1–2 μm depending on the conditions), which constricts the spatial resolution to ~0.5–1 micron, well above the typical grain size in LICGC and well above the expected scale of inhomogeneity in electrochemical behaviors (e.g. defect centers, secondary phases, etc)[12,18]. We further note that recent studies by Valov[19] and Soni[20] explore reaction mechanisms at a single location, and do not address the relationship between electrochemical reactivity and structure and morphology of the surface.

Here, we aim to elucidate the nucleation mechanism of the Li electrodeposition by studying the bias and frequency dependence (*i.e.* scan rate) of local irreversible electrochemical processes. To do so, we developed protocols to map the local nucleation potentials for Li particle formation using feedback-controlled AFM mapping modes which employ current or height-displacement cutoffs.

Results

Bias induced nucleation of Li metal under tip during reduction. Shown in Fig. 1 is the typical topography after the application of bias sweeps between 0 to−5 V resulting in the formation of Li metal

particles. It is important to mention that in this case; active cutoff feedback was turned off, allowing the bias sweep to continue despite the particle size. Note the strong variability in the particle size due to different nucleation biases at different locations. Assuming the reaction product is metallic Li, the volume of the formed particles (via topography integration) can be used to estimate the number of Li atoms deposited and is then plotted (Fig. 1b) against the number of electrons transferred (n = 1 electron transfer for $Li^+ + 1e^- \rightarrow Li_{(s)}$) in the reduction process. The slope of this graph is close to unity, suggesting that the particles formed are indeed Li metal and the electrochemical process is Li ion reduction from the glass ceramic. This analysis suggest that (a) reaction product is Li, and (b) transference number is close to 1 within the error of experiment, i.e. current passed through the tip is all converted into deposited Li. Practically, there can be reoxidation of Li (which explains loss of reversibility in air), but this process is slow and is suppressed in the glove box.

Thermodynamics of tip-induced nucleation processes. We further discuss the thermodynamics of tip-induced nucleation processes. The thermodynamic potential for the reduction of Li from Li_2O is −3.04 V. While the activity of Li_2O in LICGC can deviate from unity, the close chemical similarity between the two suggest that such deviation is minimal, while an order of magnitude change in activity changes the thermodynamic reduction by ~27 mV. The measured nucleation potentials (−3.7 ± 0.5 V in these data) hence provide a sum of intrinsic thermodynamic potential, overpotential for particle formation (local nucleation barrier for particle formation in the tip field) and ohmic (IR) drop in the material, with the latter two contributions not exceeding ~0.5 V.
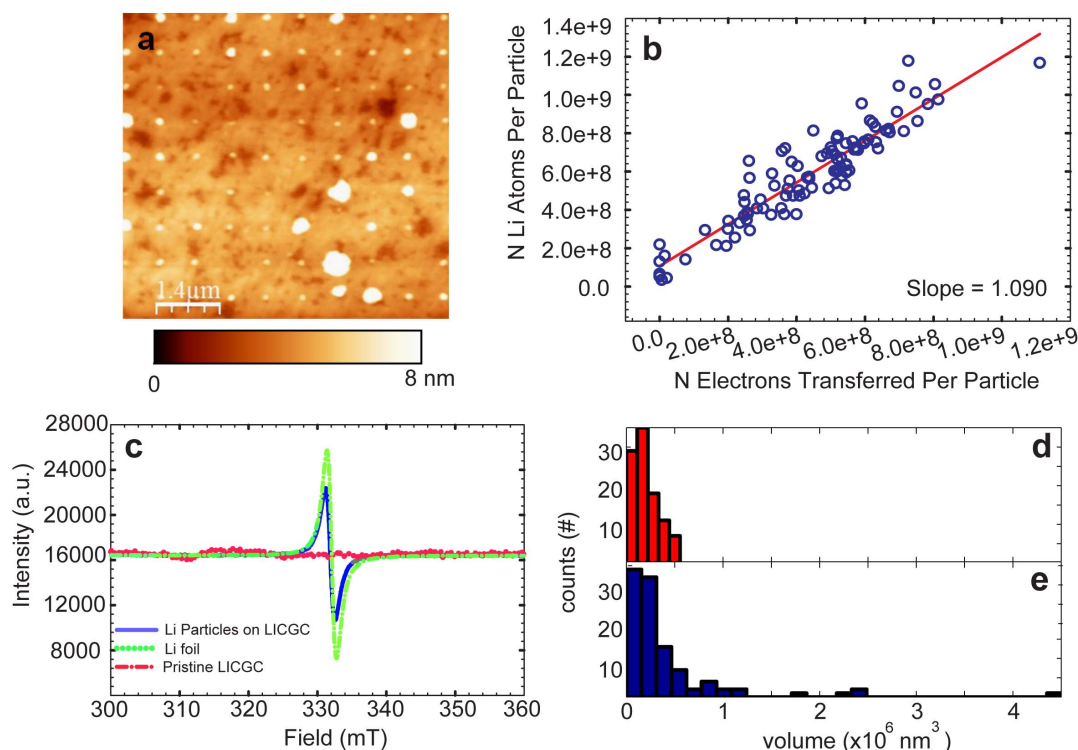

Figure 1 | Li ion reduction on LICGC using bias sweeps of 0 to −5 V (a) Li metal particles formed after the application of linear sweep from 0 V to −5 V (applied to the tip, *i.e.* tip is the working electrode) with a sweep rate of 1200 mV s⁻¹ on a 10 × 10 grid. (b) Correlation between the number of Li atoms plated and electrons transferred during the reduction. (c) Electron Paramagnetic Resonance (EPR) spectra for as received LICGC (red dash-dot line), LICGC with Li particles reduced in an Ar filled glove box (blue solid line), and Li foil (green dotted line). (d–e) Comparison of histograms of particle volume created in a normal bias sweep (blue) versus bias sweeps with current compliance (red) showing that the particles grow until a current limit is reached in compliance mode, while particles can grow uncontrollably in regular sweeps. The data in a, b and c correspond to different data sets obtained under similar conditions.

It should be noted that the particles have a wide distribution of size and there are location on the sample where the reaction does not happen at all, primarily on top of AlPO$_4$ grains (dark regions). Additionally, contrast in particle size among Li conductive regions most likely arises from the fact that different locations in the electrolyte have different nucleation potentials and Li-ion concentration. While this experiment works well to demonstrate the electrochemical reduction process, the uncontrolled formation and particles growth prevents the possibility of studying nucleation process in a spatially resolved manner on the nanoscale. For instance, application of a fixed bias (*i.e.* 5 V) at each location essentially ensures that particles *will* form (excluding the case of the tip on AlPO$_4$ grains), and in most locations they will be large (> 1 micron).

To conclusively determine the chemical nature of the deposited particles, a large array of particles (~ 5000 Li particles with average diameter ~ 2 μm) was formed in the glove box environment and hermetically sealed in quartz ampoule. Due to the dearth of analytical techniques to detect Li metal, (i.e. Energy Dispersive X-ray Spectroscopy [EDX] etc.) and necessity to maintain hermetic environment to prevent Li reaction with ambient, we chose Electron Paramagnetic Resonance (EPR). EPR is sensitive only to materials which have unpaired electrons, such as alkali metals (including Li metal), free radicals and any other chemical species with a net unpaired electron spin, while all other materials (*e.g.* Li$^+$) are EPR silent. Figure 1c shows the EPR spectra for pristine LICGC (red dash-dot line), LICGC decorated with Li particles (solid blue line) and the EPR spectrum of Li foil (green dotted line). Note that pristine LICGC produces no EPR signal in this range; while Li particle decorated LICGC produces a characteristic EPR line centered at ~ 332 mT,

which is nearly identical to that of the Li foil, identifying the particles on LICGC as Li metal.

To further explore the mechanism of the tip-induced electrochemical process, a surface was mapped by confocal micro Raman (NT-MDT) immediately after particle formation. The Raman spectrum of a particle formed upon the application of -10 V shows the emergence of a new peak in the 2700–3000 cm^{-1} frequency range as demonstrated in Fig. 2(b–d). The peak slowly increases in intensity with time. The nucleated particle can be clearly visualized in 2D Raman maps produced by the integrated peak area. The Li reaction with atmospheric oxygen and water will produce Li$_2$O and LiOH (or monohydrate LiOH.H$_2$O)[21]. The Raman spectra of these products (except for Li$_2$O which has one Raman active F$_{2g}$ mode around 525 cm^{-1}, undistinguishable from the Li$_2$O of substrate)[23] show multiple lines, including OH stretches in the 3000 cm^{-1} as well as several low frequency bands[20]. Noticeably, the Raman spectrum below 2800 cm^{-1} did not change after the particle formation, suggesting that neither LiOH or its monohydrate were formed. We assigned peaks in the 2800–3100 cm^{-1} frequency range to Li$_3$N, a product of rapid reaction of Li with molecular nitrogen[24]. A more detailed account of the Raman features and peak assignments is presented in supplemental material. We note that while these studies cannot directly identify the particle as Li (invisible in Raman during measurements performed under ambient conditions), the formation of Li$_3$N is conclusive evidence towards initial metallic state of Li.

The data in Figs. 1 and 2 allows for the identification of the (initial) reaction product as Li metal and illustrates a significant variability in reaction rate with position, rendering the question of whether the variability and nucleation mechanism can be probed on the nanometer level.
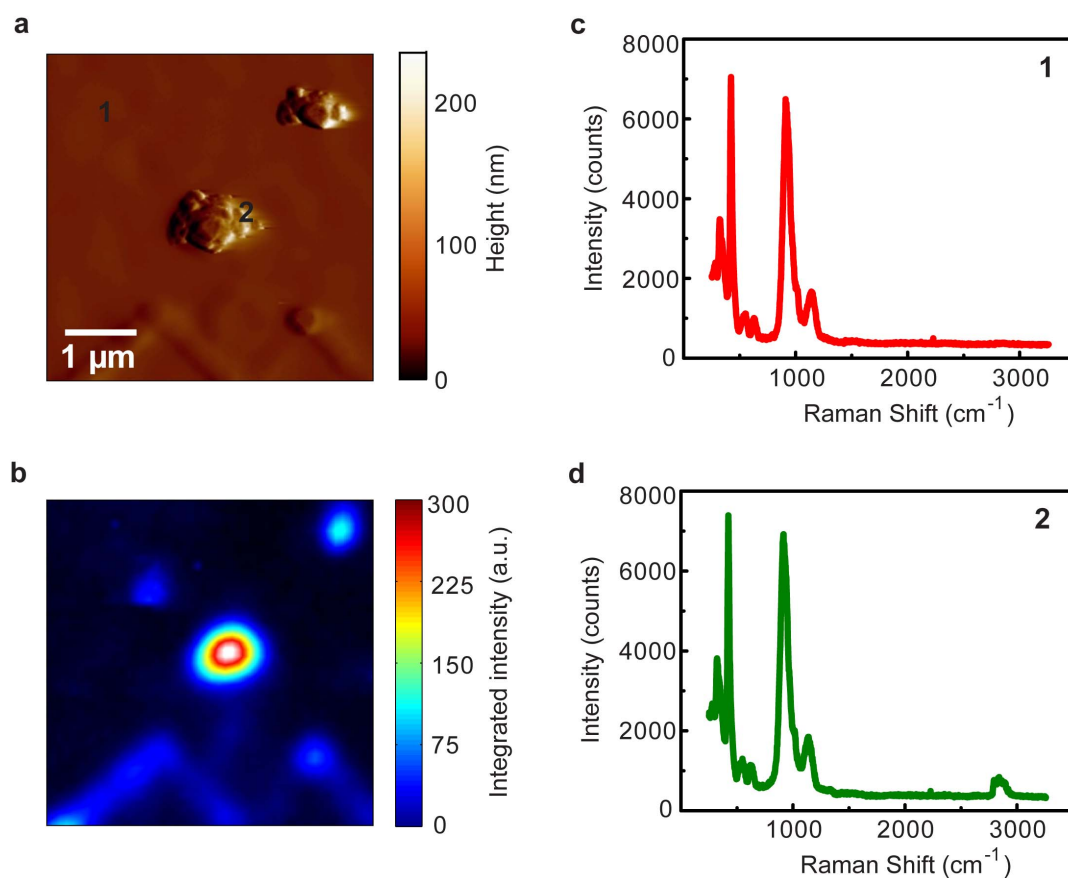

Figure 2 | Raman mapping of the Li particle (a) topography of a nucleated particle after the application of -10 V to the tip (b) Raman map of the integrated intensity for the shift in 2700–3000 cm^{-1} showing high intensity in the region of the particle (c) Raman peaks on the unbiased LICGC region compared to (d) Raman peaks on the nucleated particle.

Exploration of spatial variability of the nucleation process. To explore the spatial variability of the nucleation process, we developed a strategy based on the simultaneous detection of current and strain as the feedback mode. The application of a bias ramp to the SPM probe leads to nucleation of a Li particle and the subsequent onset of faradaic current and subsequent surface displacement detected through the SPM tip. When a predetermined compliance value was achieved (either current or tip height change), the bias ramp was aborted and the tip was moved to the next location. An active feedback is employed to terminate the electrochemical process immediately after the onset, thus precluding particles from growing further. The termination of the applied bias can be determined using either height- or current control regime, *i.e.* setting a cutoff current or a cutoff height limit. It should be noted that height control works on the basis of the detection of surface deformation whose sensitivity can be as small as a few picometers, albeit the piezo-stability and drift can in principle does in practice decrease the sensitivity.

A representative example of a single point, low density mapping using the current control approach is shown in Fig. 3. The topography measured before and after the application of the bias sweep is shown in Fig. 3 (a) and (b) respectively. Here, the particles formed by limiting the current to −10 pA illustrates much more uniform particles (lateral size and height) than in the fixed-voltage approach[15,16]. The I–V behavior of compliance is shown in Fig. 3(c) and the corresponding height change is plotted against bias in Fig. 3(d). It is clear that the onset of height change and current occurs simultaneously and the nucleation process can be studied on the nanoscale through the current or height control approach.

Current control approach to study spatially resolved nucleation. This approach is extended here to *high resolution* spatial mapping of

the electrochemical nucleation on LICGC as described below. The LICGC surface shown in Fig. 4(a) was studied with a spatial resolution of ∼ 25 nm in the current control mode. A bias sweep range of 0 V to −4.2 V_{max} was used in conjunction with a compliance cutoff of −10 pA. This approach allows us to elucidate the behavior of current at the end of a sweep (typically near the compliance cutoff value), the potential at which cutoff occurred, and the height change during nucleation recorded at each pixel as illustrated in Fig. 4(c–e). Selected I–Z curves from different locations in Fig 4(d) are shown in the supplementary material section. The topography measured after nucleation mapping (Fig. 4b) shows some modest change (surface swelling on the order of 20 nm) but the basic microstructure of the original topography was retained since the nucleation event is controlled by the compliance. These results clearly demonstrate the ability of this technique to elucidate nucleation processes and the variability of the reaction nucleation potential with microstructure in LICGC. These results demonstrate a correlation between the nucleation behavior and microstructure. Some areas on LICGC do not allow nucleation ($AlPO_4$ phase) while other regions adjacent to these phases exhibit the lowest nucleation bias. In comparison, the regions away from these phases appear to be less active thereby requiring higher bias for the Li particle nucleation.

Height control approach to study spatially resolved nucleation. It is worth noting that both current and height control can be used for nucleation detection and subsequent termination of the potential ramp. The control of nucleation using height compliance (ΔZ) is demonstrated in Fig. 5 measured over the topographical region shown in Fig. 5(a). The cutoff potential, current and height change maps are shown in Fig. 5(b–d) using a compliance cutoff of 8 nm in height change. Similar to the current control approach, the $AlPO_4$
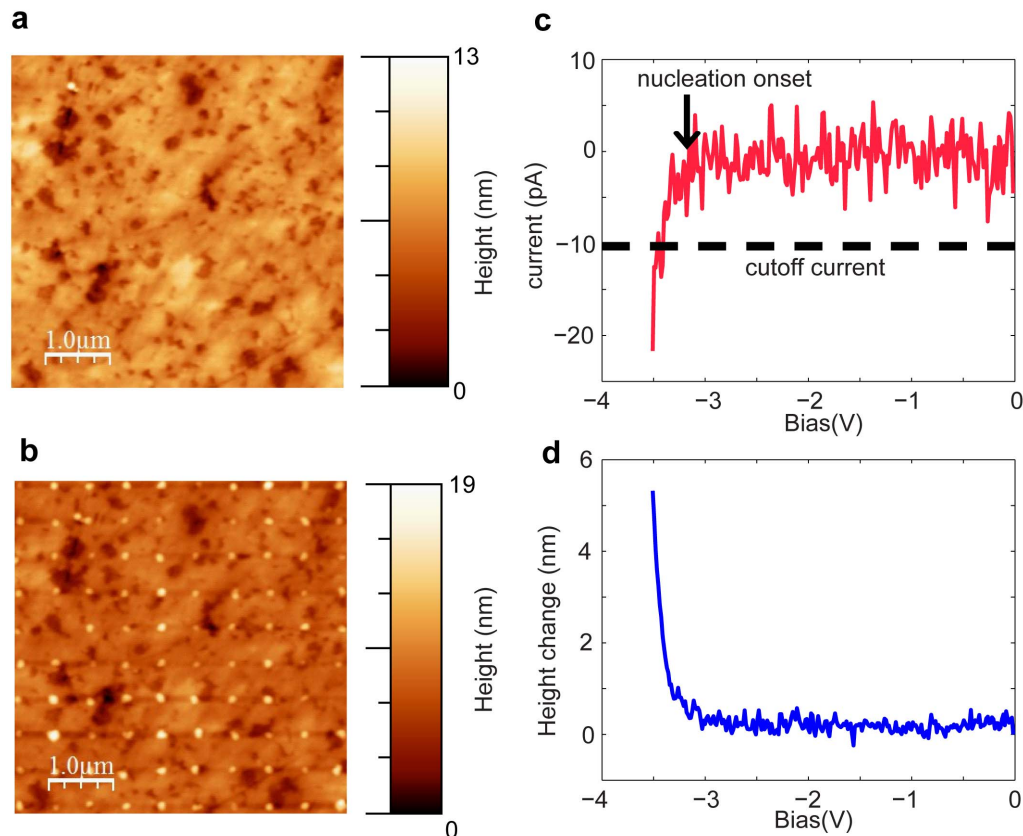

Figure 3 | Current compliance approach principle (a) AFM topography of LICGC before bias sweeps (b) AFM topography after the bias sweeps were applied on a 100 point grid, (c) I–V plot at a single location using a cutoff current set point of −10 pA (d) corresponding height change versus bias at the same surface location as (c), using a sweep rate of 1200 mV s^{-1}. The nucleation onset and the cutoff current are marked in (c).
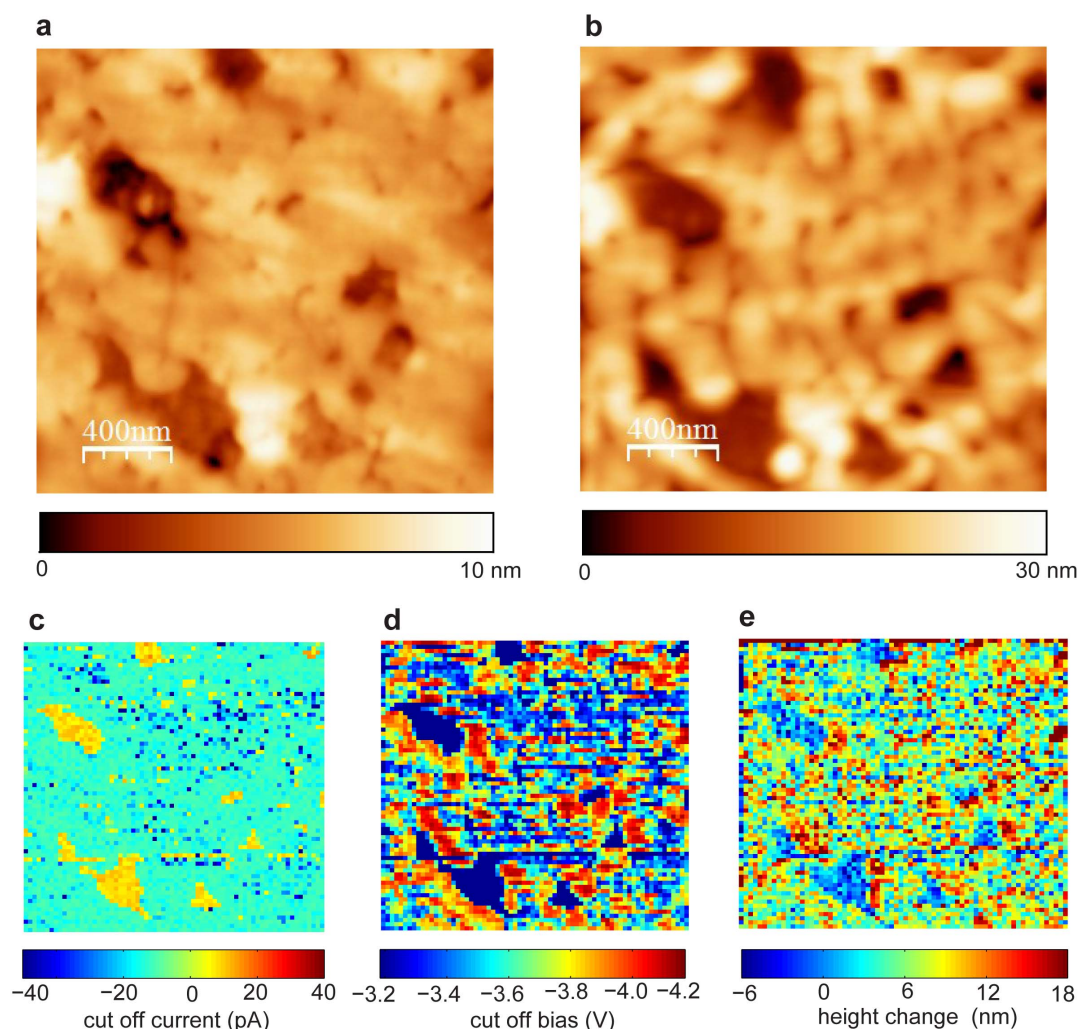
Figure 4 | Current control approach to study spatially resolved nucleation (a) AFM topography of LICGC before bias sweeps (b) AFM topography measured after the bias sweeps from 0 V to −4.2 V using a compliance of −10 pA and a 25 nm pixel resolution, (c) map of current value at the end of sweep (note that there is occasionally a single point jump that exceeds the compliance value) (d) bias at which cutoff is achieved and (e) height change maps (ΔZ) obtained from the nucleation potential/height measurement at each location.

phase does not reveal any Li particle nucleation for the entire sweep and the nucleation potential required is lower near the grain boundaries as was noted using current cutoff. These results further reiterate the observation of higher ionic conductivity near the AlPO$_4$-LICGC boundaries, which may arise due to the arguments provided above.

Note the remarkable lack of contrast in the height change map in Fig. 5(d). This map provides a good measure of the efficiency to which the active feedback turns off the bias sweep when the cutoff height is achieved. Qualitatively, the relative number of pixels which exceed ΔZ cutoff is roughly the same as that using current cutoff. However, when current cutoff was exceeded (always in a single point in the I–V curve) the cutoff value was roughly exceeded by a factor of 4. Whereas ΔZ cutoff was only exceeded by 2–4 nm, a factor of 2 at most, suggesting ΔZ cutoff may be a more sensitive approach. Finally, we note that for simple electrochemical processes such as the one explored here with only a single reaction and absence of electronic transport, both detection schemes should yield identical results.

Finite element modeling of field distribution around the AlPO$_4$-LICGC boundary. To elucidate whether the lowered nucleation potential at the interfaces arises due to field enhancement or

higher ionic concentration, the field distribution around the AlPO$_4$-LICGC boundary has been modeled. The modeling was performed using the Electrostatics module of COMSOL Finite Elements Analysis package. The model layout is displayed in Fig. 6(a). The LiCGC chip was modeled by a 1300 nm × 1200 nm × 600 nm slab with a dielectric constant $\varepsilon_{LiCGC} = 35$. The chip contained an AlPO$_4$ inclusion ($\varepsilon_{AlPO4} = 5.1$) of a hemispherical shape, flush with the upper chip surface. The radius of the inclusion is 150 nm. The tip had a conical shape with a spherical apex of a radius of 50 nm. The electrostatic potential of the bottom surface of the slab was set to zero, and a potential of 1 V was applied to the tip. The electric potential distribution was calculated for different distances between tip axis and the center of the AlPO$_4$ inclusion, δx, with the inclusion being shifted along the x-axis of the model (Figure 6(a)); at δx = 0, the center of the inclusion is on the axis of the tip. Figure 6(b) shows calculated absolute values of electric field strength within the slab versus δx, at different distances from the upper surface along the line corresponding to the tip axis. The presence of the inclusion with a lower dielectric constant has no effect on the electric field in LiCGC at distances δx > 30 nm away from the inclusion. Moreover, the electric field in LiCGC closer to the chip surface is slightly smaller, when the tip is in the vicinity of the boundary than farther away from it. This is contrary to the expected
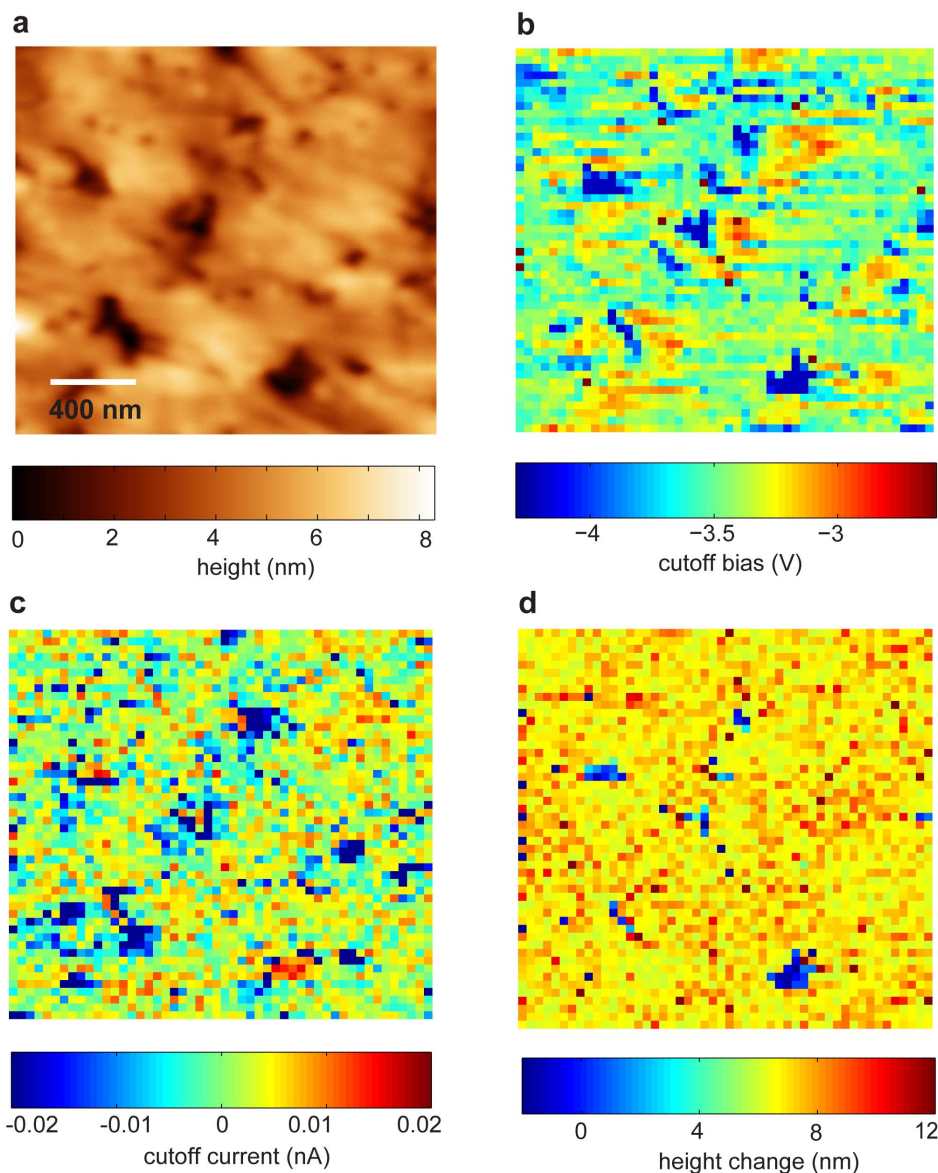
5

Figure 5 | Height control approach to study spatially resolved electrochemical nucleation processes (a) topography of LICGC before bias sweeps from 0 to −4.2 V (b) cutoff potential map (c) current at the time that height compliance was achieved (e) height change (ΔZ) map obtained from I–V–Z curves at each location. The ΔZ compliance value used was 8 nm.

result based on the experimental observations, which could be explained by an increase in the electric field strength and consequent enhancement of Li-ion electromigration. In turn, the electric field in AlPO$_4$ is noticeably increased when the tip is in the vicinity of the boundary at the AlPO$_4$ side. This is a manifestation of a known effect of "expulsion" of electric field from a higher permittivity material into an adjacent material with a smaller dielectric constant. The electrostatic potential distributions under the tip for a distance δx = 250 nm, when tip is far away from the inclusion, and for δx = 150 nm, when tip is right above the inclusion boundary, further illustrate this effect. Note, that the field drops away from the tip apex slower in the lower dielectric constant AlPO$_4$ than in LiCGC, as seen in Fig. 6(c) and (d).

Discussion

It is interesting to explore the correlation between the nucleation behavior and microstructure. While some areas on LICGC do not allow nucleation (AlPO$_4$ phase), the regions adjacent to these phases exhibit the lowest nucleation bias. The regions farther away from

these phases are less active and require higher bias for the Li particle nucleation. This situation can in principle arise because of several possible scenarios. The first is that the Li-ion concentration near the AlPO$_4$ grains is higher than in the amorphous matrix which would allow Li metal to be reduced more easily. The second possibility is that the field distribution around the AlPO$_4$ phase allows better reduction of Li ions near them (*i.e.* the AlPO$_4$ behaves like an electrocatalyst by decreasing the overpotential for reaction onset). In either case, these results suggest that ionic mobility is highest near the AlPO$_4$ grains. In fact, this effect has been previously studied by Kumar and colleagues[22,23]. They found that the presence of minor AlPO$_4$ and Li$_2$O phases contributed to a "space-charge-mediated effect," in which the mobile Li$^+$ cations adsorb and desorb to the minor phase substrate, leading to enhanced conductivity. Thus our findings agree with the noted space-charge-mediated conductivity enhancement in the vicinity of the AlPO$_4$ phases.

The relative resolution and sensitivity of the current and height control based techniques is determined by detection limits, noise levels, sample roughness and current amplifier sensitivity. While
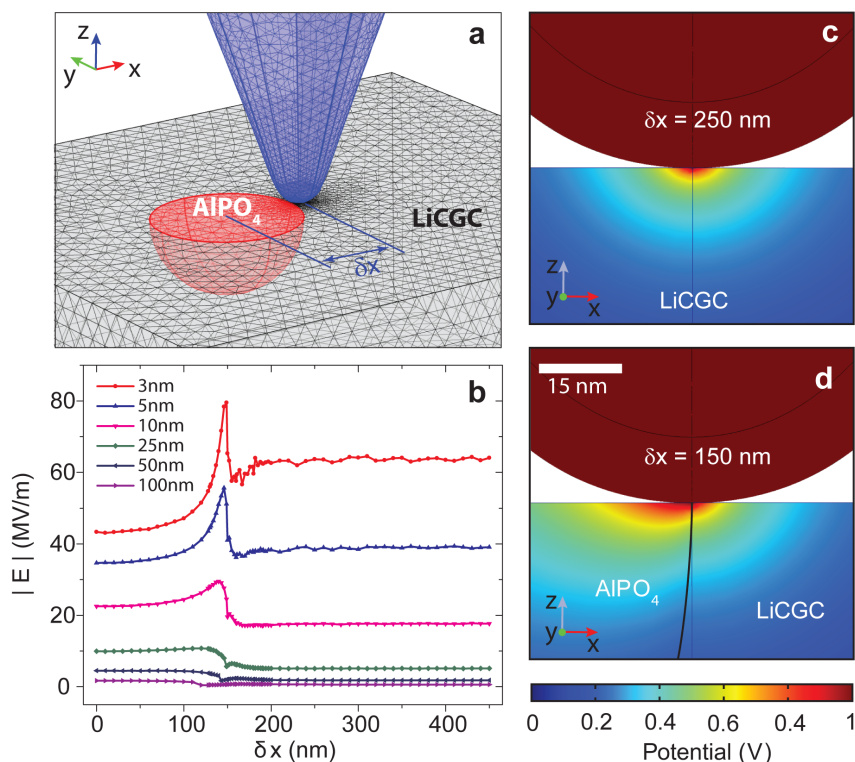
6

Figure 6 | Numerical modeling of electric field distribution under the tip. (a) Layout of the finite elements model : LiCGC slab (gray) with a hemispherical AlPO$_4$ inclusion (red) and AFM tip (blue). The radius of the inclusion is 150 nm; tip apex radius is 50 nm. (b) Absolute values of electric field strength for different distances from the upper surface of the LiCGC slab along the line corresponding to the tip axes. The field strengths were calculated as functions of the distance δx between the tip axis and the center of the AlPO$_4$ inclusion, as indicated in panel (a). The depths within the LiCGC slab are indicated in the figure legend. (c) and (d) Distribution of the electric potential in the xz-plane under the tip apex for (c) δx = 250 nm and (d) δx = 150 nm. The scale bar in (d) is common for (c) and (d).

both current and ΔZ detection show comparable resolution and sensitivity for this particular system, we note that a dynamic approach to strain detection, such as that employed in electrochemical strain microscopy (ESM) can help achieve much better height control[24,25]. In contrast, current detection limits on the order of pico-amps can be achieved, but are highly subject to ambient noise and thus more difficult to implement for reliable high-resolution control (*e.g.* monolayer scale)[16].

The results of the finite element modeling allow us to completely exclude the possibility that the contrast in Fig. 4 around the AlPO$_4$ particles can be caused by electrostatic effects associated with the vicinity of the lower dielectric constant inclusion. The dielectric effects induce only small anomalies in the field concentration, and hence cannot explain the behaviors at grain boundaries. This analysis suggests that the segregation of Li near the grains of AlPO$_4$ seems to be the most probable cause for decrease in nucleation potential.

To summarize, we have demonstrated spatially resolved mapping of the thermodynamics and kinetics of electrochemical reactivity in the irreversible Li-metal nucleation process on LICGC. The IVZ mapping allows the investigation of electrochemical nucleation potentials at the scale of ∼20 nm which is ∼ 1.5 orders of magnitude higher resolution than previously possible, and provides a pathway for studying the direct correlation between microstructure and electrochemical reactivity on the nanoscale. The enhanced electrochemical activity of the junctions between two phases was attributed to the specific adsorption of Li ions.

While the approach here has been exemplified on Li conducting glass ceramics (LICGC), it can be extended to the detailed study any solid state ionic conductor for mapping of ionic motion/concentration and phase nucleation via electrochemical reaction in other

systems. We note that recent advances in fields such as molecular unfolding spectroscopy has provided insight into the kinetics and thermodynamics of reactions on a single molecule level, and believe that this approach will provide comparable information for reactions in solids on a level of single defect or structural element. As such, it can be universally applicable for material systems such as fuel cell materials, memristors, and many others.

Methods

Electron paramagnetic resonance spectra. All EPR spectra were collected at 233 K in sealed, Ar filled quartz EPR tubes. EPR scan parameters for the Li foil and Li decorated LICGC are as follows: B-field modulation 500 mG, microwave attenuation: 10 dB using a gain of 10; the pristine LICGC scan employed a modulation raised stepwise to 2000 mG and the gain was raised stepwise to 200 to confirm the absence of signal.

Electrochemical cell configuration. In all cases, metal coated (Pt [Budget Sensors Multi75E-G, k = 3 N m^{-1}] and in some cases diamond coated tips [DCP20, k = 28 – 91 N m^{-1}, NT-MDT]) AFM tip served as the working electrode to which bias was applied. In general, the studies performed with conductive diamond coated tips revealed comparable results to the Pt tips, with the advantage of using diamond coated tips being durability. The LICGC plate (AG-01, Ohara Inc.) was mounted to a Cu counter electrode and connected via a conductive coating (colloidal Ag paint, Ted Pella Inc.). Thus a two electrode setup was employed and the potentials measured in these experiments were versus a mixed potential reference (Cu/Cu$^{+/2+}$ + Ag/Ag$^+$). Though it is possible to use a Li-foil counter/reference electrode, this configuration is preferable due to the propensity of LICGC to react with Li[15].

Current and height compliance implementation. Atomic Force Microscopy measurements were performed with a commercial system (Asylum Research Cypher) additionally equipped with LabView/MatLab based band excitation controller implemented on a NI-6115 DAQ card. Mapping of the current and height compliance was done typically on a 70 × 70 points grid with a spacing of 20 nm, albeit other spacing and image sizes were also used. All measurements were performed with the biased tip in direct contact with the LICGC surface.

7

1. Fuechsle, M. *et al.* A single-atom transistor. *Nature Nanotech.* **7**, 242–246 (2012).
2. Shao, Y. *et al.* Making Li-Air Batteries Rechargeable: Material Challenges. *Adv. Func. Mat.* **23**, 987–1004 (2013).
3. Madden, J. D. W. *et al.* Fast carbon nanotube charging and actuation. *Adv. Mat.* **18**, 870–873 (2006).
4. Baughman, R. H. Playing nature's game with artificial muscles. *Science* **308**, 63–65 (2005).
5. Garcia, R. *et al.* Nanopatterning of carbonaceous structures by field-induced carbon dioxide splitting with a force microscope. *App. Phys. Lett.* **96**, 143110 (2010).
6. Cen, C. *et al.* Nanoscale control of an interfacial metal-insulator transition at room temperature. *Nat. Mater.* **7**, 298–302 (2008).
7. Yang, J. J. *et al.* The mechanism of electroforming of metal oxide memristive switches. *Nanotechnology* **20**, 215201 (2009).
8. Garcia, R., Martinez, R. V. & Martinez, J. Nano-chemistry and scanning probe nanolithographies. *Chem. Soc. Rev.* **35**, 29–38 (2006).
9. Maupai, S., Zhang, Y. & Schmuki, P. Nanoscale observation of initial stages of Cd-electrodeposition on Au(111). *Surf. Science* **527**, L165–L170 (2003).
10. Martinez, R. V., Losilla, N. S., Martinez, J., Tello, M. & Garcia, R. Sequential and parallel patterning by local chemical nanolithography. *Nanotechnology* **18**, 084021 (2007).
11. Lee, M., O'Hayre, R., Prinz, F. B. & Gur, T. M. Electrochemical nanopatterning of Ag on solid-state ionic conductor RbAg4I5 using atomic force microscopy. *App. Phys. Lett.* **85**, 3552–3554 (2004).
12. Kruempelmann, J., Balabajew, M., Gellert, M. & Roling, B. Quantitative nanoscopic impedance measurements on silver-ion conducting glasses using atomic force microscopy combined with impedance spectroscopy. *Solid State Ionics* **198**, 16–21 (2011).
13. Fu, J. Fast Li$^+$ ion conducting glass-ceramics in the system Li$_2$O–Al$_2$O$_3$–GeO$_2$–P$_2$O$_5$. *Solid State Ionics* **104**, 191–194 (1997).
14. Fu, J. Superionic conductivity of glass-ceramics in the system Li$_2$O–Al$_2$O$_3$–TiO$_2$–P$_2$O$_5$. *Solid State Ionics* **96**, 195–200 (1997).
15. Kraytsberg, A. & Ein-Eli, Y. Review on Li-air batteries-Opportunities, limitations and perspective. *J. Power Sources* **196**, 886–893 (2011).
16. Arruda, T. M., Kumar, A., Kalinin, S. V. & Jesse, S. Mapping Irreversible Electrochemical Processes on the Nanoscale: Ionic Phenomena in Li Ion Conductive Glass Ceramics. *Nano Lett.* **11**, 4161–4167 (2011).
17. Arruda, T. M., Kumar, A., Kalinin, S. V. & Jesse, S. The partially reversible formation of Li-metal particles on a solid Li electrolyte: applications toward nanobatteries. *Nanotechnology* **23**, 325402 (2012).
18. Kruempelmann, J. *et al.* Nanoscale electrochemical measurements on a lithium-ion conducting glass ceramic: In-situ monitoring of the lithium particle growth. *Electrochem. Comm.* **18**, 74–77 (2012).
19. Valov, I. *et al.* Atomically controlled electrochemical nucleation at superionic solid electrolyte surfaces. *Nature Mater.* **11**, 530–5 (2012).
20. Soni, R. *et al.* On the stochastic nature of resistive switching in Cu doped Ge$_{0.3}$Se$_{0.7}$ based memory devices. *J. App. Phys.* **110**, 054509 (2011).
21. Chandrasekhar, H. R., Bhattacharya, G., Migoni, R. & Bilz, H. Infrared and Raman-Spectra and Lattice-Dynamics of Superionic Conductor Li$_3$N. *Phys. Rev. B* **17**, 884–893 (1978).
22. Kumar, B., Nellutla, S., Thokchom, J. S. & Chen, C. Ionic conduction through heterogeneous solids: Delineation of the blocking and space charge effects. *J. Power Sources* **160**, 1329–1335 (2006).
23. Kumar, B., Thomas, D. & Kumar, J. Space-Charge-Mediated Superionic Transport in Lithium Ion Conducting Glass–Ceramics. *J. Electrochem. Soc.* **156**, A506–A513 (2009).
24. Kumar, A., Ciucci, F., Morozovska, A. N., Kalinin, S. V. & Jesse, S. Measuring oxygen reduction/evolution reactions on the nanoscale. *Nature Chem.* **3**, 707–713 (2011).
25. Balke, N. *et al.* Nanoscale mapping of ion diffusion in a lithium-ion battery cathode. *Nature Nanotech.* **5**, 749–754 (2010).

Author contributions

A.K. and S.V.K. proposed the concept. S.J. and A.K. designed the experiments. A.K. and T.M.A. performed the experiments. The Raman measurements were done by I.N.I., O.B. and S.Z. J.S.L. and T.A.Z. performed the EPR measurements. The numerical calculations were performed by A.T. A.K., T.M.A. and S.V.K. wrote the article. All authors discussed the results and commented on the manuscript.

Additional information

Supplementary information accompanies this paper at http://www.nature.com/scientificreports

How to cite this article: Kumar, A. *et al.* Nanometer-scale mapping of irreversible electrochemical nucleation processes on solid Li-ion electrolytes. *Sci. Rep.* **3**, 1621; DOI:10.1038/srep01621 (2013).